metals

MDPI

Article

Investigation of Ti6Al4V Alloy Fabricated by LPBF with Thick Layer: Role of Scanning Speed in Defect Control and Mechanical Performance

Zixiang Qiu [1,2,3], Haixuan Wang [1,2], Shimin Fang [2], Yongjian Zheng [2], Shuyi Liu [2], Chaoyue Tang [2], Qizhong Huang [2] and Hao Zhang [2,*]

[1] Qianwan Institute of CNITECH, Ningbo 315336, China; qizixiang@nimte.ac.cn (Z.Q.); wanghaixuan@nimte.ac.cn (H.W.)
[2] Ningbo Institute of Materials Technology and Engineering, Chinese Academy of Sciences, Ningbo 315201, China; fangshimini@nimte.ac.cn (S.F.); yongjian.zheng@nimte.ac.cn (Y.Z.); liushuyi@nimte.ac.cn (S.L.); tangchaoyuei@nimte.ac.cn (C.T.); huangqizhong@nimte.ac.cn (Q.H.)
[3] State Key Laboratory of Advanced Marine Materials, Ningbo Institute of Materials Technology and Engineering, Chinese Academy of Sciences, Ningbo 315201, China
* Correspondence: haozhang@nimte.ac.cn

Abstract

Aiming at the contradiction between forming quality and efficiency in the existing research on thick-layer laser powder bed fusion (LPBF) manufacturing of Ti6Al4V, this study focused on the influence of near-circular keyhole defects caused by scanning speed on the short-term mechanical properties of Ti6Al4V alloy manufactured by high-efficiency LPBF with a 100 μm layer thickness, the build rate of which reached 14 mm^3/s. When the scanning speed decreased to 800 mm/s, the relative density decreased from 99.87% to 99.27%, and the maximum pore size increased from 19.6 μm to 87.2 μm. Under the conditions of high relative density (above 99.8%) and maximum pore size less than 20 μm, the annealed Ti6Al4V samples could achieve a tensile strength of 1009.7 MPa, a yield strength of 914.0 MPa, an elongation of 15.2%, and an impact toughness of 41.71 J/cm^2. With the increase in porosity and a maximum pore size exceeding 50 μm, the tensile strength became more unstable and exhibited a declining trend, while the impact toughness decreased by more than 5%. This is mainly attributed to the stress concentration around large-sized pores, leading to the easy generation of long and deep cracks at the edges and reducing the material's ability to resist crack initiation and propagation.

Keywords: LPBF; Ti6Al4V alloy; large layer thickness; scanning speed

Check for updates

Academic Editor: Manoj Gupta

Received: 12 February 2026
Revised: 2 March 2026
Accepted: 5 March 2026
Published: 6 March 2026

Copyright: © 2026 by the authors. Licensee MDPI, Basel, Switzerland. This article is an open access article distributed under the terms and conditions of the Creative Commons Attribution (CC BY) license.

1. Introduction

As a core technology in the field of metal additive manufacturing, laser powder bed fusion (LPBF) has become an important means for manufacturing complex metal components in high-end fields such as aerospace, medical care, and energy, due to its characteristics of high forming accuracy, high part relative density, excellent surface quality, and strong ability to form complex structures [1–5]. Ti6Al4V alloy, as the most widely used titanium alloy in current LPBF technology, combines high specific strength, excellent corrosion resistance, and good bio-compatibility, and is used to manufacture important components in key fields such as aerospace (airframe bolts, engine fan casings), medical care (orthopedic implants, dental restorations), and chemical industry (corrosion-resistant pipeline components) [6–9].

However, low productivity has severely restricted the application of LPBF-fabricated Ti6Al4V components. Traditional LPBF processes mostly adopt a thin layer thickness of 20–50 μm, resulting in a low build rate of 0.5–4.5 mm^3/s [10], which makes it difficult to meet the mass production demand for large components in the aerospace field. In recent years, many studies have shown that increasing the powder layer thickness of the LPBF process can significantly improve the build rate and break the productivity bottleneck. Wang et al. [11] prepared 316L stainless steel by LPBF with a 150 μm layer thickness, and the relative density of the component could reach 99.99% under optimal parameters, with a build rate of 12 mm^3/s, which is 3–10 times that of the traditional thin-layer process. Chauhan et al. [12] compared the effects of 30 μm and 60 μm layer thicknesses on additive-manufactured Ti6Al4V and found that although the 60 μm layer thickness led to a 16% decrease in elongation, the building efficiency was nearly doubled, and the tensile strength was still higher than that of forged Ti6Al4V. Ludwig et al. [13] further verified that when using coarse powder with a particle size of 45–106 μm combined with a 60 μm layer thickness, not only is the raw material cost reduced by 38–44% compared with fine powder of 20–53 μm, but also the relative density of Ti6Al4V components can be maintained above 99.9% through parameter optimization. In addition, Singla et al. [7] pointed out that the essence of productivity improvement in thick-layer LPBF is achieved by reducing the number of powder spreading times and scanning layers. When the layer thickness increased from 30 μm to 200 μm, the number of forming layers for components with the same height decreased from 33 to 5, which greatly shortened the process cycle. Regarding the LPBF process of Ti6Al4V in a thick layer, recent studies have made considerable progress focusing on process parameter optimization and defect control, and good mechanical properties have been obtained. Brudler et al. [14] took the dimensionless Fourier number (Fo) as the core of regulation, and in the layer thickness range of 60–300 μm, using a laser with maximum power of 400 W and beam diameter ranging of 62–300 μm with negative defocus matching the layer thickness, determined Fo = 1.25 and laser power 380 W as the optimal parameters to make the relative density of each layer thickness reached 99.99%. The build rate reached 8.76 mm^3/s at the 300 μm layer thickness. However, more incomplete fusion defects occurred at this layer thickness, and the composite defects of keyhole pores and incomplete fusion led to a serious decrease in elongation, which was only 2%. Another study also found that excessively large powder layer thickness will lead to an unavoidable significant decrease in elongation [15]. Further research found that by comparing 50 μm and 200 μm beam diameters, the 200 μm large spot can significantly reduce molten pool spatter, thereby achieving a relative density of 99.95% at a 200 μm layer thickness, an elongation increased to 8.02%, and a maximum build rate of 9 mm^3/s. Even so, small-sized spherical micro-pores are still unavoidable, which is mainly due to the rapid solidification of the molten pool leading to the failure of argon to escape [16].

At present, research on LPBF processing of Ti6Al4V in a thick layer has covered parameter optimization, defect control, and performance characterization. It can be found that under the condition of a maximum laser power of 500 W for mainstream LPBF metal printers, a 100 μm layer thickness is the optimal matching layer thickness for forming quality and efficiency. As shown in Table 1, the limitation of existing research is that excessive pursuit of full density (>99.99%) leads to a significant reduction in the scanning speed (below 120 mm/s) to achieve a low defect rate after increasing the powder layer thickness, thereby limiting the improvement of the build rate. This study employed LPBF processing of Ti6Al4V at a layer thickness of 100 μm at high scanning speeds, with a density requirement of only above 99%, achieving the highest build efficiency reported to date. The effect of a certain number of keyhole defects on the tensile and impact properties

of LPBF-fabricated Ti6Al4V alloy was investigated, providing a reference for balancing forming quality and build efficiency in industrial production.

Table 1. Overview of scanning speeds, layer thickness, and corresponding build rates of LPBF-fabricated Ti6Al4V in the literature.

Ref.	Scanning Speed	Layer Thickness	Build Rate
[10]	60 mm/s	200 μm	7.20 mm^3/s
[14]	119 mm/s	120 μm	5.50 mm^3/s
[14]	60 mm/s	240 μm	7.32 mm^3/s
[14]	48 mm/s	300 μm	8.77 mm^3/s
[16]	100 mm/s	200 μm	9.00 mm^3/s

2. Materials and Methods

2.1. Material and LPBF Parameters

The Ti6Al4V powder used in this study was provided by Shangcai 3D Technology Co., Ltd. (Ningbo, China). The powder was prepared by gas atomization, with a particle size range of 15–53 μm, which is suitable for LPBF fabrication. The SEM morphology of the powder is shown in Figure 1. The chemical composition of the powder is listed in Table 2, which meets the chemical composition standard for LPBF-fabricated Ti6Al4V powder. The powder was dried in a vacuum furnace at 110 °C for 4 h before the LPBF process.

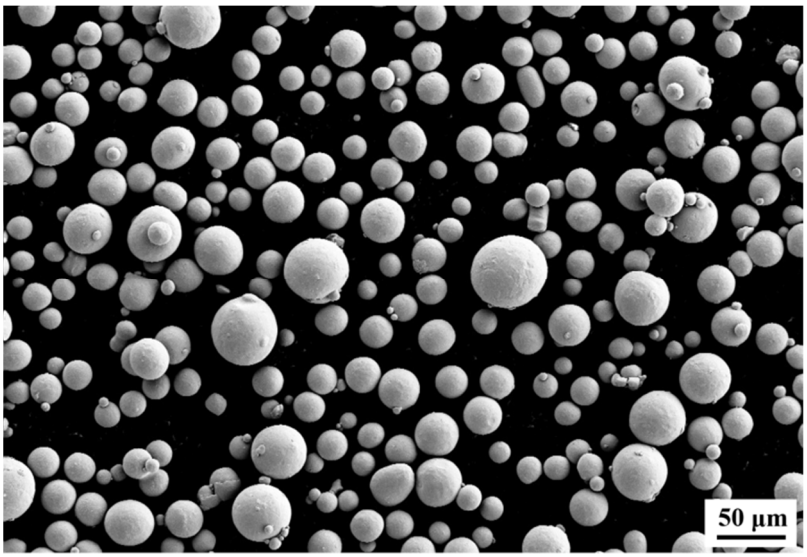


Figure 1. SEM morphology of Ti6Al4V powder.

Table 2. Chemical composition of Ti6Al4V powder.

Elements	Al	V	Fe	C	H	O	N
wt%	5.84	3.96	0.03	<0.01	<0.01	0.08	<0.01

The printing equipment used was an HBD-E400 metal 3D printer produced by Hanbang Laser Technology Co., Ltd. (Zhongshan, China), with a maximum laser power of 500 W and a spot diameter of 50 μm. The entire printing process was carried out under an argon protective atmosphere, and the oxygen concentration in the forming chamber was lower than 800 ppm. The LPBF process parameters are shown in Table 3. An in-layer path planning strategy with 5 mm-wide strips was adopted; the inter-layer rotation angle was

67°, and the substrate preheating temperature was 100 °C. Under these process parameters, the maximum build rate can reach 14.0 mm^3/s, exceeding the build rate reported recently.

Table 3. LPBF parameters of the samples.

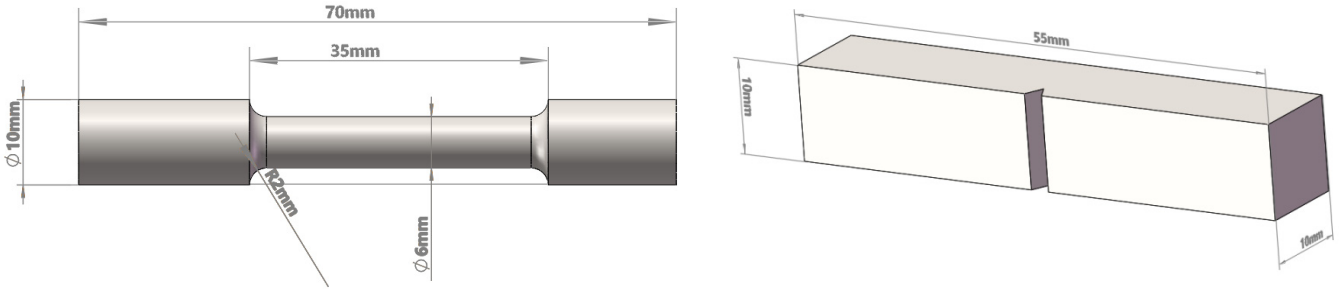
Scanning Speed	Laser Power	Hatch Distance	Layer Thickness	VED	Build Rate
1000 mm/s	350 W	0.14 mm	100 µm	25.0 J/mm^3	14.0 mm^3/s
900 mm/s	350 W	0.14 mm	100 µm	27.8 J/mm^3	12.6 mm^3/s
800 mm/s	350 W	0.14 mm	100 µm	31.3 J/mm^3	11.2 mm^3/s

2.2. Heat Treatment and Microstructure Characterization

After the LPBF process, to eliminate the residual stress introduced in the samples during the rapid solidification process, the samples were subjected to stress-relief annealing at 800 °C for 2 h, in accordance with the heat treatment routine for Ti6Al4V. The samples were separated from the substrate using wire electrical discharge machining (WEDM). Then, the six surfaces of the test blocks (size: 10 × 10 × 12 mm) were ground smooth with sandpaper, and the relative density of the test blocks was measured by the Archimedes method to evaluate the forming quality. Subsequently, the test blocks were embedded and polished with thermosetting resin, and the internal defects were directly observed using a metallographic microscope (Axio Observer, Carl Zeiss AG, Oberkochen, Germany). To observe the microstructures and phase distributions of the formed samples, these specimens were etched for 15 s with Keller's reagent (1 mL HF, 1.5 mL HCl, 2.5 mL HNO_3, and 95 mL H_2O), and microstructure observation was performed using a scanning electron microscope (GEMINI 300, Carl Zeiss AG, Oberkochen, Germany).

2.3. Mechanical Property Characterization

Tensile property tests were carried out at room temperature using standard-sized samples specified in GB/T 228.1-2021 [17], with specimen dimensions illustrated in Figure 2a. A tensile testing machine (Z600E, ZwickRoell, Ulm, Germany) was used for the tests, following the tensile rate standard specified in GB/T 228.1-2021. Each tensile test was performed three times, and the average value was taken.



(**a**) (**b**)

Figure 2. (**a**) Tensile test rod; (**b**) impact test rod.

Impact property tests were carried out at room temperature using standard-sized V-notch samples specified in GB/T 229-2020 [18], with specimen dimensions illustrated in Figure 2b. A pendulum impact testing machine (HIT450P, ZwickRoell, Ulm, Germany) was used for the tests, following the standard of GB/T 229-2020. Each impact test was performed three times, and the average value was taken.

3. Results and Discussion

3.1. Relative Density

The relative density measured by the Archimedes method significantly decreased with the decrease in scanning speeds, which were 99.87%, 99.48%, and 99.27%, respectively, as shown in Table 4. The XOZ surfaces of the three samples were ground and polished to directly observe the pore defects. The distribution of defects on the XOZ plane was macroscopically observed using low-magnification metallographic micrographs, and the results are shown in Figure 3. Samples fabricated at the scanning speed of 1000 mm/s had a few defects. As the scanning speed decreased, both the size and number of defects increased significantly, resulting in large defects being distributed on the XOZ plane of samples prepared at scanning speeds of 900 mm/s and 800 mm/s, with these large defects being relatively evenly distributed across the entire XOZ plane. Figure 4 shows the metallographic structures of the samples fabricated at three different scanning speeds, and the selected fields of view are the parts with the densest pores on the ground and polished surfaces. It can be found that the pores caused by the low scanning speed are mainly circular and elliptical, with regular shapes. The porosity increased significantly with the decrease in scanning speed, so the number of pores observed at the same magnification also obviously increased. At the same time, the size of the largest pore in the field of view also increased significantly with the decrease in scanning speed. At the scanning speed of 1000 mm/s, the maximum pore size was less than 20 μm. The maximum pore size was less than 50 μm at the scanning speed of 900 mm/s, while the maximum pore size exceeded 80 μm at the scanning speed of 800 mm/s. During the laser melting of the powder bed, when the energy input is sufficiently high, the keyhole effect is likely to occur. Under the influence of the Marangoni effect, the gas stirred into the bottom of the keyhole is trapped by the solidified metal before it can escape, resulting in keyhole defects. A thicker powder layer produces deeper keyholes than conventional layer thickness, thus increasing the probability of gas pore trapping [19]. Moreover, with a certain power, the deeper the keyholes generated in the molten pool at a lower scanning speed, the more likely the keyhole defects are to occur [20]. The superposition of the two led to high porosity.

Table 4. Relative density and largest pore size.

Scanning Speed	Relative Density/%	Largest Pore Size/μm
1000 mm/s	99.87	19.6
900 mm/s	99.48	49.1
800 mm/s	99.27	87.2

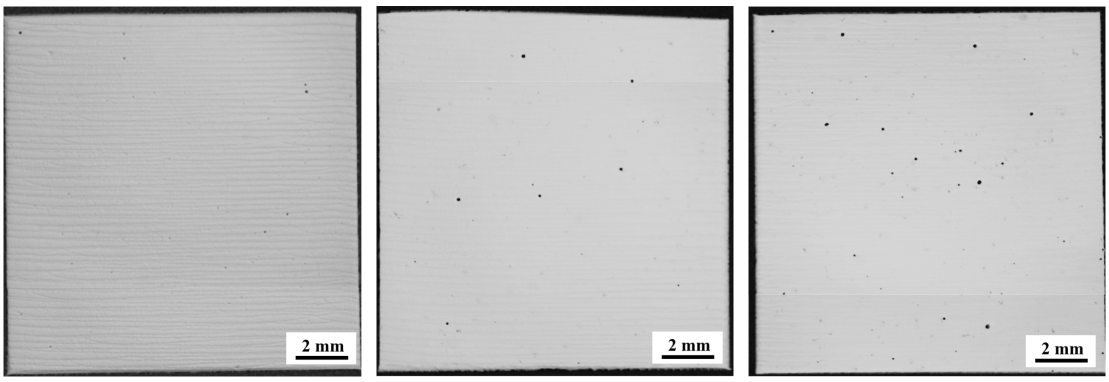


Figure 3. Macrostructures of samples (XOZ surfaces) fabricated at different scanning speeds: (**a**) 1000 mm/s; (**b**) 900 mm/s; and (**c**) 800 mm/s.

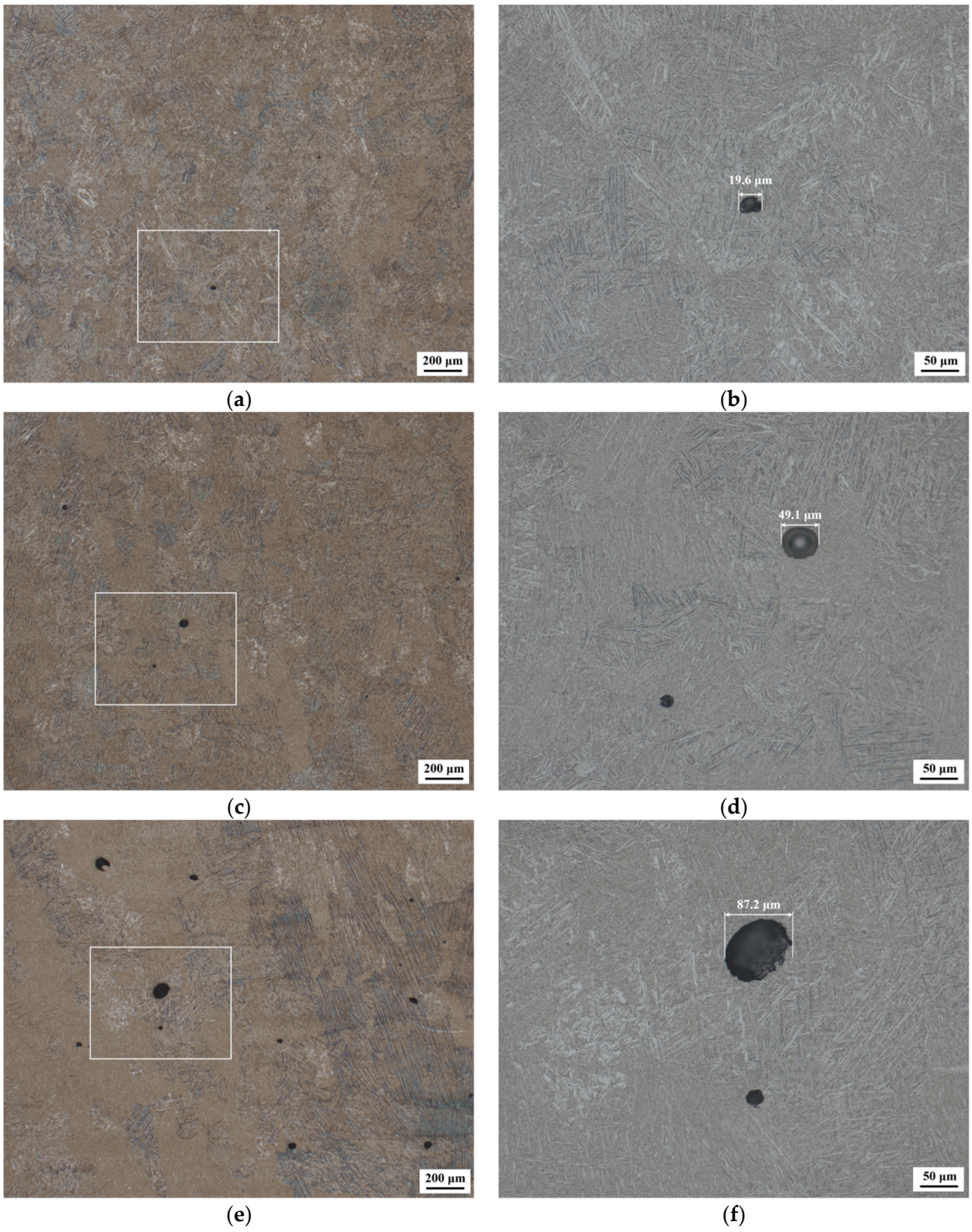


Figure 4. OM images of samples fabricated at different scanning speeds: (**a**) 1000 mm/s, 50×; (**b**) 1000 mm/s, 200×; (**c**) 900 mm/s, 50×; (**d**) 900 mm/s, 200×; (**e**) 800 mm/s, 50×; and (**f**) 800 mm/s, 200×.

3.2. Microstructures

The Ti6Al4V alloy directly processed by LPBF contained a large amount of α′ acicular martensite, as shown in Figure 5a, which had an adverse effect on plasticity. To be closer to engineering applications, this study adopted a vacuum-annealing heat treatment regime of 800 °C for 2 h, which can obtain a titanium alloy with balanced strength and plasticity [21]. The SEM microstructures after heat treatment are shown in Figure 5b–d. The α′ acicular

martensite structure in the samples after vacuum annealing had been broken and decomposed, gradually transforming into short acicular martensite α′ phase, and long strip α phase and secondary β phase began to appear, presenting a typical basketweave structure. The degree of martensite coarsening at the three scanning speeds was comparable, and no significant differences in microstructures were observed.

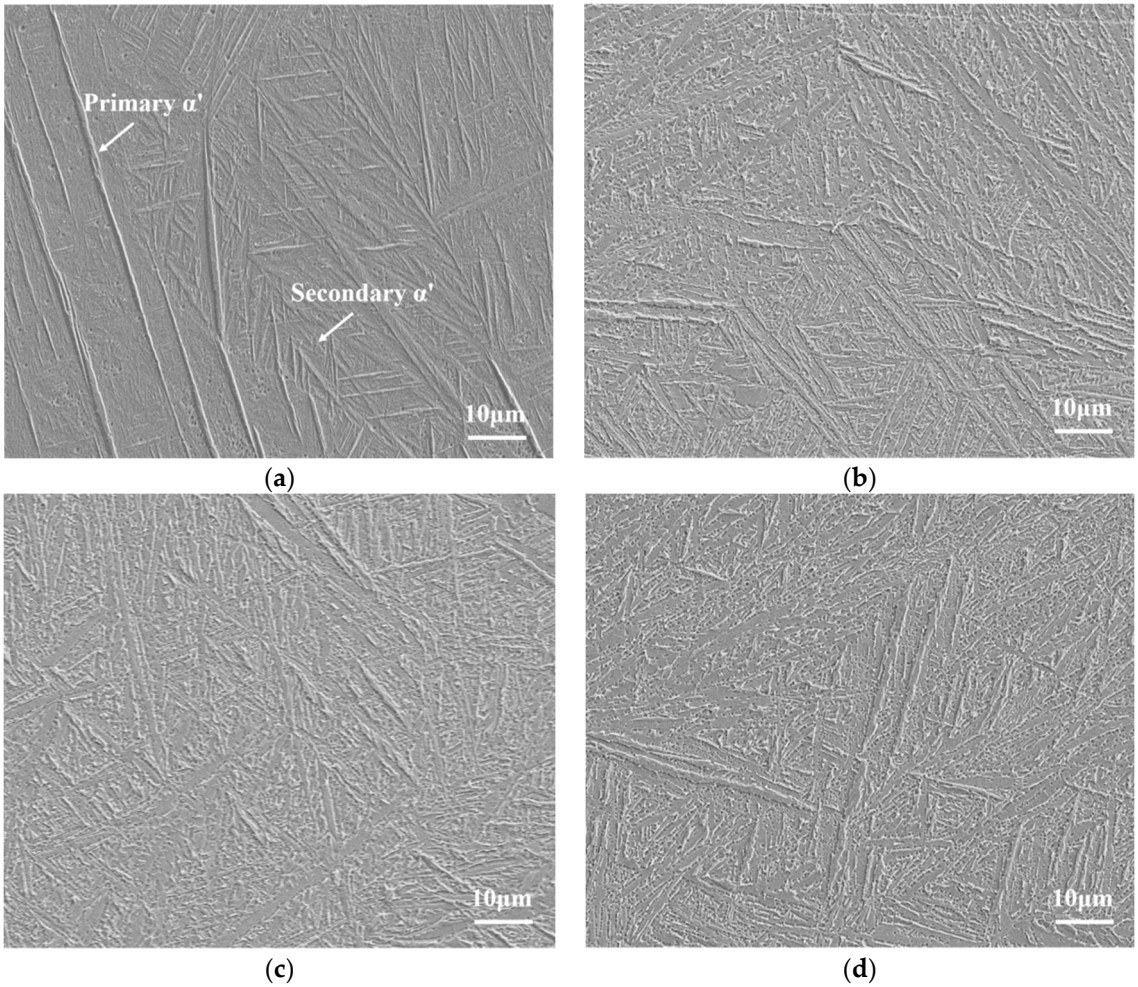


Figure 5. SEM micrographs (**a**) as-fabricated sample fabricated at the scanning speed of 1000 mm/s; samples fabricated at the scanning speed of (**b**) 1000 mm/s, (**c**) 900 mm/s, and (**d**) 800 mm/s after annealing.

3.3. Tensile Properties

Figure 6 and Table 5 show the tensile properties of the samples at different scanning speeds. The average values and standard deviations of the tensile properties are shown in Figure 6b, while the data of all three tensile tests are presented in Table 5. It could be observed that the effect of porosity on the short-term tensile strength is mainly reflected in decreasing the tensile property stability, which easily leads to abrupt drops in performance among the same batch of samples. The samples fabricated at a scanning speed of 1000 mm/s exhibited excellent mechanical property stability, with the difference between the maximum and minimum strength values being less than 15 MPa, and that between the maximum and minimum elongation values being less than 1%. In contrast, the samples prepared at scanning speeds of 800 mm/s and 900 mm/s showed much larger variations in strength and elongation, where the difference between the maximum and minimum strength values exceeded 30 MPa, and that between the maximum and minimum elongation values was

more than 2%. For the samples at a scanning speed of 800 mm/s, the difference between the maximum and minimum elongation values even exceeded 3%.

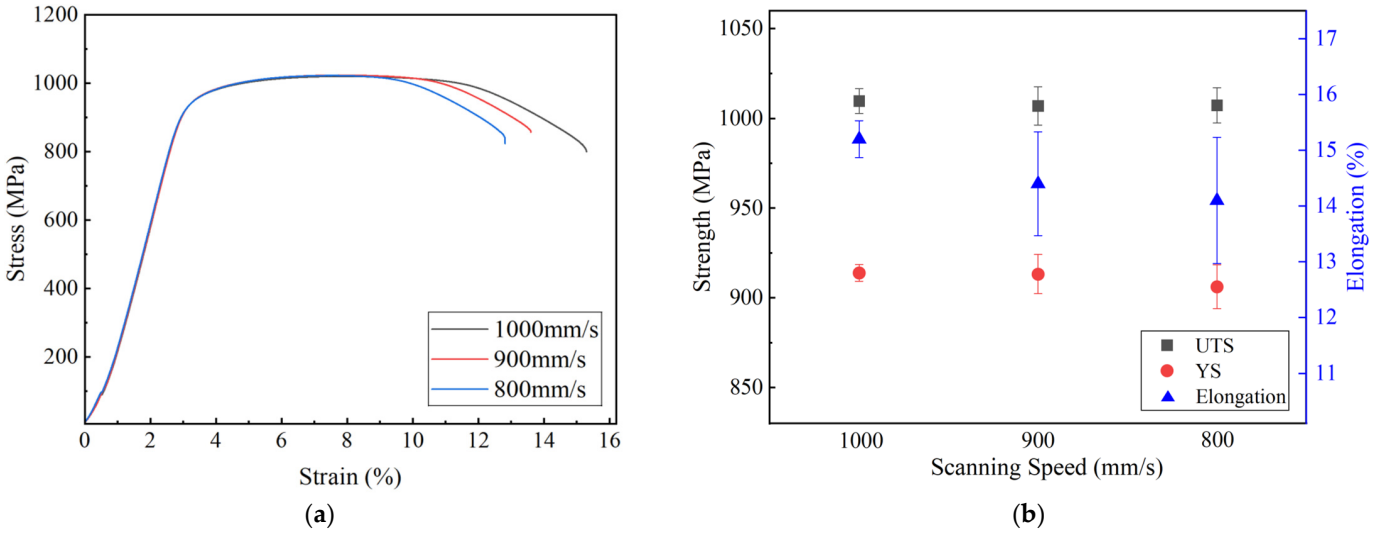


Figure 6. Tensile properties of samples: (**a**) stress–strain curves of samples at different scanning speeds (strain rate: 0.0003 s^{-1}), and (**b**) average rates of tensile properties.

Table 5. Tensile properties of samples fabricated at different scanning speeds.

Scanning Speed	UTS/MPa	YS/MPa	Elongation/%
1000 mm/s	1004	907	15.5
	1020	920	15.4
	1005	915	14.7
900 mm/s	1001	914	13.8
	1023	929	15.8
	997	897	13.6
800 mm/s	1002	911	12.7
	1022	920	15.8
	998	888	13.8

To further explain the tensile test data, fracture analysis was performed on the tensile samples with scanning speeds of 1000 mm/s and 800 mm/s. Despite certain differences in mechanical properties, both scanning speeds show certain similarities in their fracture behavior. Both samples exhibited cup–cone fractures, characterized by fine tear ridges (an indicator of ductility) and dense small dimples near their centers, showing ductile fracture characteristics.

The difference was that the fracture surface of the sample at 1000 mm/s showed very few spherical defects (as shown in Figure 7a), while the fracture surface of the sample at 800 mm/s showed a large number of spherical defects (as shown in Figure 7b), which can be identified as keyhole pores of different sizes, confirming the observation in Figure 4e. Observing the 500× magnified fracture surface in Figure 7d, cracks were found around the keyhole pores, and the fracture surface around the keyhole pores showed brittle fracture characteristics. This indicated that keyhole defects larger than 20 μm acted as crack sources during tensile deformation, promoting crack initiation, which also explained the decrease in elongation of the samples at 900 mm/s and 800 mm/s. When observed at 1000× magnification (as shown in Figure 7f), cracks at the fracture surface were significantly easier

to find in the sample at the scanning speed of 800 mm/s, which also led to an obvious loss of yield strength of the sample processed at this scanning speed.

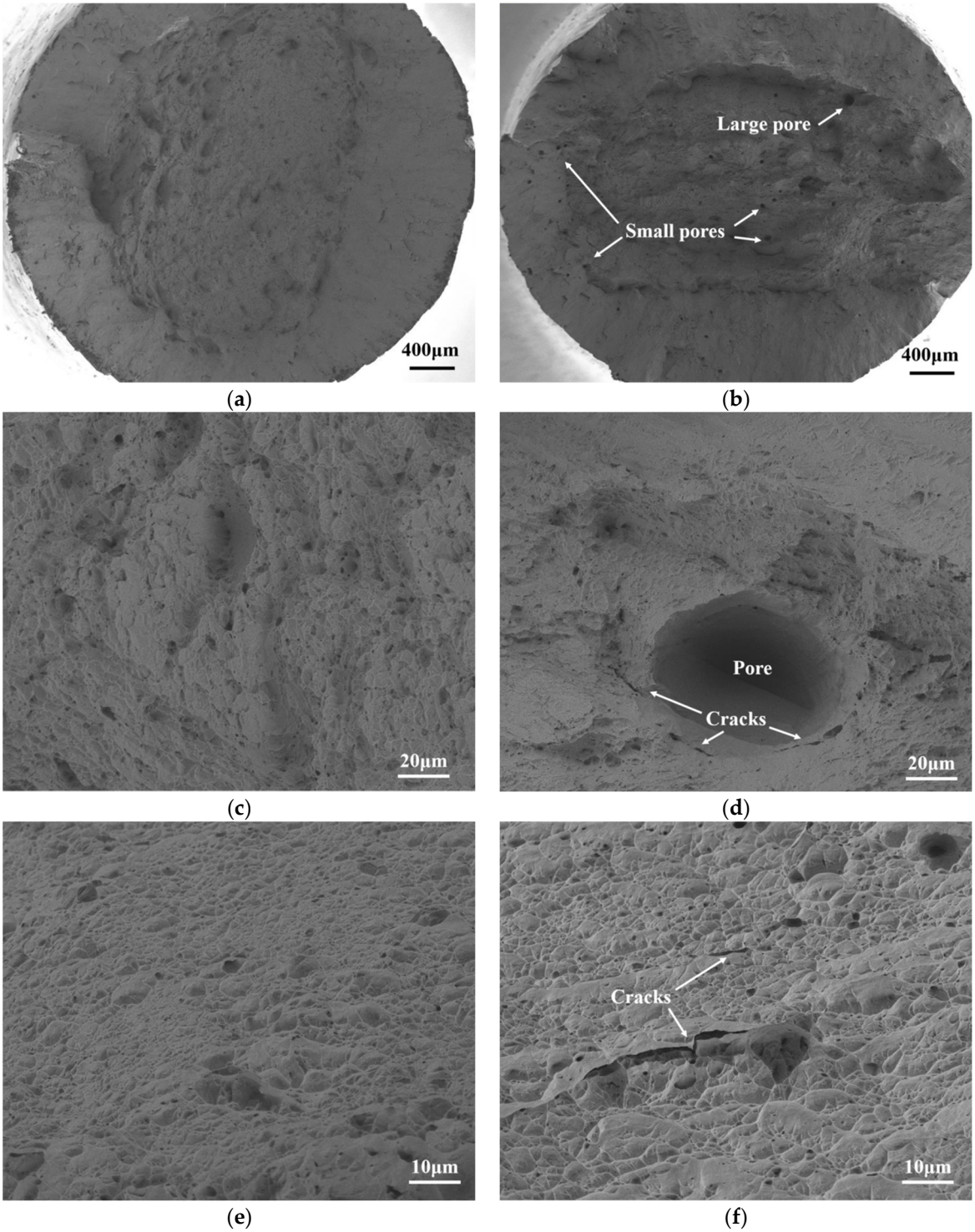


Figure 7. Tensile fracture morphology of samples (**a**) 1000 mm/s, 50×; (**b**) 800 mm/s, 50×; (**c**) 1000 mm/s, 200×; (**d**) 800 mm/s, 200×; (**e**) 1000 mm/s, 500×; and (**f**) 800 mm/s, 500×.

3.4. Impact Toughness

To further investigate the effect of pores generated at low scanning speeds on mechanical properties, impact tests were also performed on the three samples, and the results are shown in Table 6. The impact toughness of the samples processed at scanning speeds

of 1000 mm/s, 900 mm/s, and 800 mm/s is 41.71 J/cm^2, 39.10 J/cm^2, and 39.13 J/cm^2 respectively. The results showed that pores also have an adverse effect on the impact performance of the samples. Compared with the sample processed at the scanning speed of 1000 mm/s, the impact energy and impact toughness of the samples processed at the scanning speeds of 900 mm/s and 800 mm/s both obviously decreased, with a decrease of more than 5%.

Table 6. Impact toughness properties of the samples.

Scanning Speed	W/J	a_k/J·cm^{-2}
1000 mm/s	33.37 ± 0.37	41.71 ± 0.46
900 mm/s	31.28 ± 0.05	39.10 ± 0.06
800 mm/s	31.30 ± 0.79	39.13 ± 0.98

The main factors affecting the impact toughness of the alloy are the energy required for crack initiation and crack propagation in the structure. Therefore, impact toughness is essentially the ability of the material to resist crack initiation and crack propagation. The factors that determine the energy required for crack initiation and propagation differ substantially. The crack initiation energy is proportional to the plastic deformation degree at the notch position of the alloy, while the crack propagation energy is usually proportional to the tortuosity of the crack propagation path. It has also been reported in the literature [22] that the plastic deformation degree generated in the crack propagation zone is smaller than that in the crack initiation zone, because the local misorientation in the crack propagation zone is much lower than that in the crack initiation zone. Even the easily deformable β phase does not produce severe plastic deformation, indicating that the plastic deformation during crack propagation is much smaller. Therefore, the energy consumed by plastic deformation during crack propagation is much lower than that consumed during crack initiation. In the analysis of tensile properties in Section 3.3, we already know that pores will promote crack initiation, so they are also unfavorable to the impact performance of the material. For the Ti6Al4V alloy prepared by LPBF with a 100 μm-thick layer in this study, the defects show a distinct distribution characteristic dependent on scanning speed, and the pore size and number density increase significantly with the decrease in scanning speed, which is shown in Figure 3. This specific defect distribution leads to a different probability of interaction between the stress field around the V-notch, the initial stress concentration zone of the impact sample, and internal pores. At the scanning speed of 1000 mm/s, the small pore size and low number density result in a low interaction probability between the notch stress field and pores. Thus, crack initiation is still dominated by the plastic deformation at the notch, and the required initiation energy remains high. In contrast, at low scanning speeds of 800 and 900 mm/s, the larger pores and higher number density increase the interaction probability between the notch stress field and internal defects. The pores act as secondary stress concentration sources overlapping with the notch stress field, which significantly reduces the plastic deformation degree required for crack initiation and the corresponding energy barrier, thus accelerating the crack initiation process and further deteriorating the impact toughness of the alloy.

Crack initiation energy dominates the total fracture energy of the alloy [23,24]. Therefore, careful observation of the fracture surface to find possible crack sources can help us understand the fracture mechanism. The fracture surfaces of the impact samples were observed by scanning electron microscopy, and Figure 8 shows the micrographs of the fracture surfaces after the impact toughness test. The crack initiation, propagation, and shear tip regions can be clearly observed. The microfracture of the sample processed at the scanning speed of 1000 mm/s was covered with dimples and large flat cleavage facets,

and no obvious traces of keyhole defects were observed, as shown in Figure 8a,b. In contrast, a large number of keyhole defects can be clearly observed on the microfractures of the samples processed at the scanning speeds of 900 mm/s and 800 mm/s, and the pore diameter of the sample processed at 800 mm/s is obviously larger than that of the sample processed at 900 mm/s. Further observation found that long and deep cracks were more likely to be found at the edges of keyhole defects larger than 20 μm. The grain size around pore defects is significantly smaller than that of the solid regions adjacent to these defects. This sudden change in grain size has been proven to facilitate local crack propagation and reduce the threshold stress intensity, leading to stress concentration and crack nucleation around the pores, which has a significant impact on the mechanical properties of the structural components [25]. Therefore, the impact toughness of the samples processed at the scanning speeds of 900 mm/s and 800 mm/s was significantly lower than that of the sample processed at 1000 mm/s with lower porosity.

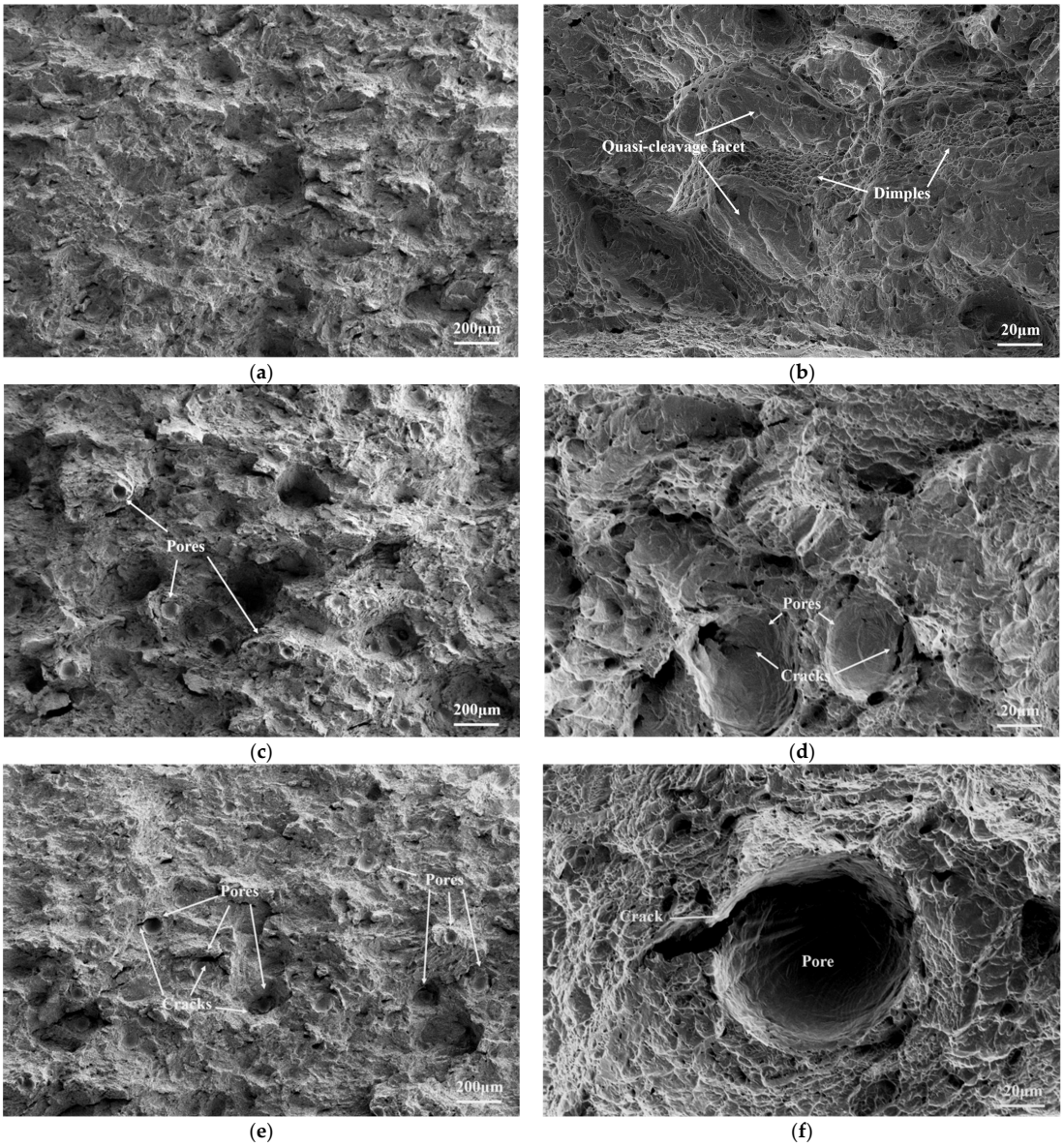


Figure 8. Impact fracture morphology of samples (**a**) 1000 mm/s, 50×; (**b**) 1000 mm/s, 200×; (**c**) 900 mm/s, 50×; (**d**) 900 mm/s, 200×; (**e**) 800 mm/s, 50×; and (**f**) 800 mm/s, 200×.

4. Conclusions

This study systematically investigated the influence of scanning speed on the porosity, microstructure, and mechanical properties, including tensile properties and impact toughness, of Ti6Al4V alloy processed by LPBF, and optimized the properties by combining a heat treatment process of vacuum annealing at 800 °C for 2 h. The core conclusions are as follows:

- Scanning speed has a significant regulatory effect on the porosity and maximum pore size of the alloy. As the scanning speed decreases from 1000 mm/s to 800 mm/s, the porosity measured by the Archimedes method decreases from 99.87% to 99.27%, and the maximum pore size increases from 19.6 μm to 87.2 μm. The mechanism is that the superposition of a thick layer and low scanning speed enhances the keyhole effect, making it difficult for gas to escape and form defects.
- As-fabricated Ti6Al4V via LPBF contained a large amount of acicular α′ martensite, which impairs plasticity. After annealing at 800 °C for 2 h, it transformed into a basketweave structure to achieve the balance of strength and plasticity. The degree of martensite coarsening after annealing at different scanning speeds was similar, and no significant difference in microstructure morphology was observed.
- High porosity reduces the tensile property stability, with the fluctuation of tensile strength and elongation within the same batch of samples increasing as the scanning speed decreases. The strength variation is less than 15 MPa, and the elongation variation is below 1% for the sample fabricated at 1000 mm/s, while the strength variation exceeds 30 MPa and the elongation variation is over 2% for the samples fabricated at 800 and 900 mm/s.
- The impact toughness of samples processed at scanning speeds of 900 mm/s and 800 mm/s decreases by more than 5% compared with that of 1000 mm/s. This is because the stress concentration around large-sized pores will lead to the easy generation of long and deep cracks at the edges, reducing the material's ability to resist crack initiation and propagation.

Author Contributions: Conceptualization, H.Z. and Z.Q.; methodology, Q.H. and H.Z.; software, C.T.; validation, S.L., S.F. and Y.Z.; formal analysis, C.T. and H.W.; investigation, Q.H.; resources, S.F.; data curation, S.L.; writing—original draft preparation, Z.Q.; writing—review and editing, Z.Q. and H.W.; visualization, H.W.; supervision, Y.Z.; project administration, Q.H. and Y.Z.; funding acquisition, H.Z. All authors have read and agreed to the published version of the manuscript.

Funding: This research was funded by the "Pioneer" and "Leading Goose" R&D Program of Zhejiang, China (grant numbers: 2023C01053; 2024C01121); and the Yongjiang talent introduction programmer (2021A-112-G; 2022A-202-G); international partnership program of the Chinese Academy of Sciences, grant no.181GJHZ2023132ML.

Data Availability Statement: The original contributions presented in this study are included in the article. Further inquiries can be directed to the corresponding author.

Conflicts of Interest: The authors declare no conflicts of interest.

References

1. Chowdhury, S.; Yadaiah, N.; Prakash, C.; Ramakrishna, S.; Dixit, S.; Gupta, L.R.; Buddhi, D. Laser powder bed fusion: A state-of-the-art review of the technology, materials, properties & defects, and numerical modelling. *J. Mater. Res. Technol.* **2022**, *20*, 2109–2172. [CrossRef]
2. Nandhakumar, R.; Venkatesan, K. A process parameters review on selective laser melting-based additive manufacturing of single and multi-material: Microstructure, physical properties, tribological, and surface roughness. *Mater. Today Commun.* **2023**, *35*, 105538. [CrossRef]

3. Ren, Z.H.; Zhang, H.; Shu, X.D.; Xu, H.J.; Chen, S.Y.; Ding, Y.Y.; Liang, L.W.; Qiu, Z.X.; Yang, Y.; Zheng, Y.J. Study on microstructure and high-temperature mechanical properties of Al-Mg-Sc-Zr alloy processed by LPBF. *Metals* **2024**, *14*, 890. [CrossRef]
4. Yang, C.S.; Huang, B.; Zheng, Y.J.; Li, J.H.; Zhang, H.; Ding, Y.Y.; Liang, L.W.; Qiu, Z.X.; Wang, H.X.; Yang, Y.; et al. Influence of heat treatment on the microstructural evolution of CoCrFeNi high-entropy alloy prepared by selective laser melting. *J. Mater. Res. Technol.* **2025**, *35*, 4920–4928. [CrossRef]
5. Kong, Z.Y.; Deng, T.S.; Zhang, H.; Zheng, Y.J.; Qiu, Z.X.; Huang, Q.Z.; Wang, H.X.; Yang, Y.; Ding, Y.Y.; Liang, L.W.; et al. Microstructure, mechanical properties at room temperature and high temperature of TC17 titanium alloy fabricated by laser powder bed fusion. *Mater. Sci. Eng. A* **2025**, *947*, 149143. [CrossRef]
6. Liu, S.Y.; Shin, Y.C. Additive manufacturing of Ti6Al4V alloy: A review. *Mater. Des.* **2019**, *164*, 107552. [CrossRef]
7. Singla, A.K.; Banerjee, M.; Sharma, A.; Singh, J.; Bansal, A.; Gupta, M.K.; Khanna, N.; Shahi, A.S.; Goyal, D.K. Selective laser melting of Ti6Al4V alloy: Process parameters, defects and post-treatments. *J. Manuf. Process.* **2021**, *64*, 161–187. [CrossRef]
8. Bartolomeu, F.; Gasik, M.; Silva, F.S.; Miranda, G. Mechanical Properties of Ti6Al4V Fabricated by Laser Powder Bed Fusion: A Review Focused on the Processing and Microstructural Parameters Influence on the Final Properties. *Metals* **2022**, *12*, 986. [CrossRef]
9. Ni, C.B.; Zhu, J.J.; Zhang, B.G.; An, K.; Wang, Y.Q.; Liu, D.J.; Lu, W.; Zhu, L.D.; Liu, C.F. Recent advance in laser powder bed fusion of Ti–6Al–4V alloys: Microstructure, mechanical properties and machinability. *Virtual Phys. Prototyp.* **2025**, *20*, e2446952. [CrossRef]
10. Shi, X.; Ma, S.; Liu, C.; Chen, C.; Wu, Q.; Chen, X.; Lu, J. Performance of large layer thickness in Selective Laser Melting of Ti6Al4V. *Materials* **2016**, *9*, 975. [CrossRef]
11. Wang, S.; Liu, Y.; Shi, W.; Qi, B.; Yang, J.; Zhang, F.; Han, D.; Ma, Y. Research on large layer thickness Fabricated of 316L by Selective Laser Melting. *Materials* **2017**, *10*, 1055. [CrossRef]
12. Chauhan, A.K.S.; Shukla, M.; Kumar, A. Insights into microstructure and mechanical properties of 3D printed Ti-6Al-4V alloy at different layer thicknesses. *Mater. Lett.* **2025**, *384*, 138047. [CrossRef]
13. Ludwig, I.; Kluge, M. Investigation of an Increased Particle Size Distribution of Ti-6Al-4V Powders Used for Laser-Based Powder Bed Fusion of Metals. *Materials* **2024**, *17*, 2942. [CrossRef]
14. Brudler, S.; Medvedev, A.E.; Pandelidi, C.; Piegert, S.; Illston, T.; Qian, M.; Brandt, M. Systematic investigation of performance and productivity in laser powder bed fusion of Ti6Al4V up to 300 μm layer thickness. *J. Mater. Process. Technol.* **2024**, *330*, 118450. [CrossRef]
15. Shi, X.Z.; Yan, C.; Feng, W.W.; Zhang, Y.L.; Leng, Z. Effect of large layer thickness on surface quality and defect behavior of Ti-6Al-4V fabricated by selective laser melting. *Opt. Laser Technol.* **2020**, *132*, 106471. [CrossRef]
16. Shi, W.; Liu, Y.; Shi, X.; Hou, Y.; Wang, P.; Song, G. Beam Diameter Dependence of Performance in Thick-Layer and High-Power Selective Laser Melting of Ti-6Al-4V. *Materials* **2018**, *11*, 1237. [CrossRef] [PubMed]
17. *GB/T 228.1-2021*; Metallic Materials—Tensile Testing—Part 1: Method of Test at Room Temperature. China Standards Press: Beijing, China, 2021.
18. *GB/T 229-2020*; Metallic Materials—Charpy Pendulum Impact Test Method. China Standards Press: Beijing, China, 2020.
19. Ma, M.M.; Wang, Z.M.; Gao, M.; Zeng, X.Y. Layer thickness dependence of performance in high-power selective laser melting of 1Cr18Ni9Ti stainless steel. *J. Mater. Process. Technol.* **2015**, *215*, 142–150. [CrossRef]
20. Cunningham, R.; Zhao, C.; Parab, N.; Kantzos, C.; Pauza, J.; Fezzaa, K.; Sun, T.; Rollett, A.D. Keyhole threshold and morphology in laser melting revealed by ultrahigh-speed x-ray imaging. *Science* **2019**, *363*, 849–852. [CrossRef] [PubMed]
21. Xiao, M.L.; Zan, L.; Ke, L.D.; Deng, Z.J.; Lai, C.F.; Sun, J.L. Effect of Annealing Process on Microstructure and Room-Temperature Mechanical Properties of Laser Powder Bed Fusion Fabricated Ti6Al4V Alloy. *Heat Treat. Met.* **2020**, *45*, 108–112. [CrossRef]
22. Wu, C.; Zhao, Y.Q.; Huang, S.X.; Lei, L.; Zhao, Q.Y.; Sun, Q.Y.; Zhou, L. Microstructure tailoring and impact toughness of a newly developed high strength Ti-5Al-3Mo-3V-2Cr-2Zr-1Nb-1Fe alloy. *Mater. Charact.* **2021**, *175*, 111103. [CrossRef]
23. Wen, X.; Wan, M.P.; Huang, C.W.; Tan, Y.B.; Lei, M.; Liang, Y.L.; Cai, X. Effect of microstructure on tensile properties, impact toughness and fracture toughness of TC21 alloy. *Mater. Des.* **2019**, *180*, 107898. [CrossRef]
24. Xu, J.W.; Zeng, W.D.; Zhao, Y.W.; Jia, Z.Q. Effect of microstructure evolution of the lamellar alpha on impact toughness in a two-phase titanium alloy. *Mater. Sci. Eng. A* **2016**, *676*, 434–440. [CrossRef]
25. Pang, J.F.; Huang, L.M.; Liu, H.L.; Yi, X. Melt pool dynamics and pore formation in selective laser melting: Mechanisms and microstructural insights. *Mater. Des.* **2025**, *254*, 114043. [CrossRef]

Disclaimer/Publisher's Note: The statements, opinions and data contained in all publications are solely those of the individual author(s) and contributor(s) and not of MDPI and/or the editor(s). MDPI and/or the editor(s) disclaim responsibility for any injury to people or property resulting from any ideas, methods, instructions or products referred to in the content.